Journal Pre-proofs

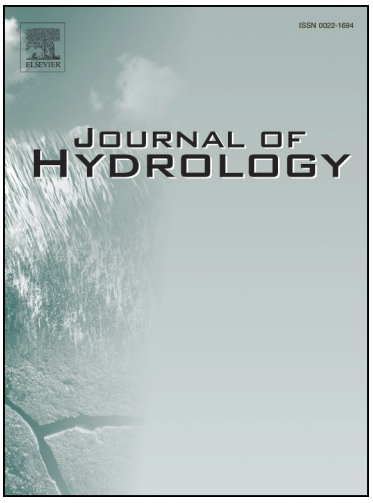

Research papers

Reporting nanoparticle tracers: Validation of performance in flow-through experiments simulating reservoir conditions

Jonathan Berson, Bastian Rudolph, Laura Spitzmüller, Thomas Kohl, Thomas Schimmel

PII: S0022-1694(24)00824-2
DOI: https://doi.org/10.1016/j.jhydrol.2024.131429
Reference: HYDROL 131429

To appear in: *Journal of Hydrology*

Received Date: 30 March 2024
Revised Date: 8 May 2024
Accepted Date: 12 May 2024

Please cite this article as: Berson, J., Rudolph, B., Spitzmüller, L., Kohl, T., Schimmel, T., Reporting nanoparticle tracers: Validation of performance in flow-through experiments simulating reservoir conditions, *Journal of Hydrology* (2024), doi: https://doi.org/10.1016/j.jhydrol.2024.131429

Reporting Nanoparticle Tracers: Validation of Performance in Flow-Through Experiments Simulating Reservoir Conditions

Jonathan Berson[a,b] (*), Bastian Rudolph[a,b,c] , Laura Spitzmüller [a,b,c], Thomas Kohl[c] and Thomas Schimmel[a,b]

* Corresponding author, e-mail address: jonathan.berson@kit.edu

Affiliations:

a)

Institute of Nanotechnology, Karlsruhe Institute of Technology

Hermann-von-Helmholtz-Platz 1

76344 Eggenstein-Leopoldshafen, Germany

b)

Institute of Applied Physics, Karlsruhe Institute of Technology

Wolfgang-Gaede-Straße 1, 76131 Karlsruhe, Germany

c)

Institute of Applied Geosciences, Division of Geothermal

Energy & Reservoir Technology, Karlsruhe Institute of Technology

Adenauerring 20b, 76131 Karlsruhe, Germany

Keywords:

Nanoparticle tracers, Flow-through, Packed-bed column, Smart tracers, Stimuli-responsive tracers, Tracer sorption

Abstract

Characterization and monitoring of reservoir properties and conditions are key problems in the exploitation of subsurface aquifers and reservoirs, with tracer tests being an important tool that provides valuable insights into groundwater dynamics. The Reporting Nanoparticle Tracers (RNTs) approach was recently presented with the aim of expanding the scope of measureable parameters and the potential benefits of tracer tests in comparison to tests performed with traditional tracers. However, successful implementation of the concept depends on the ability of the nanoparticle tracers to exhibit a stable dispersion that facilitates sufficiently high recovery rates to allow for meaningful analysis. As a step forward toward the implementation of the approach, we used flow-through studies with packed-bed quartz sand columns to compare the transport and retention properties of the RNTs with those of prevalent conservative molecular tracers and to show the feasibility of temperature detection. In the main experiments, the RNTs showed recovery rates around 80%, outperformed only by uranine (95%) and surpassing eosin and sulforhodamine G (15% and 50% respectively). Thermally-activated RNTs could also be clearly differentiated from non-activated ones by a signal ratio difference of 50%. These results validate the feasibility of application, especially considering the modularity of the nanoparticles, which enables adjustment of the RNTs to the hydrochemical conditions prevalent in the tested aquifer.

1. Introduction

Reporting Nanoparticle Tracers (RNTs) have been introduced as a novel approach to expand and enhance the scope, capabilities and applicability of subsurface tracer tests (Rudolph et al., 2020). Determining and characterizing aquifer properties such as hydrodynamic behavior (Fronzi et al., 2020), contaminations (Gasser et al., 2010) or solute transport (Sarris et al., 2018), as well as geothermal reservoir properties such as temperature, pH level or salinity, are of utmost importance for the evaluation of a reservoir for its suitability and profitability of production (Ju et al., 2020; Witter et al., 2019). Moreover, reservoir characterization is vital for monitoring its stability after water or energy production from an aquifer had commenced (Olasolo et al., 2016; Salley et al., 2022). While the most direct way to measure reservoir properties is by performing downhole measurements at drilled boreholes in selected points across the reservoir (Hsieh et al., 2021), these measurements provide data that are restricted to the direct vicinity of the borehole, are limited by the high expenses and difficulty of drilling boreholes and might be distorted by the drilling activity itself (Kruszewski and Wittig, 2018). Unlike the local nature of the data obtained by downhole measurements, tracer testing yields comprehensive information about an entire section of the reservoir (Zhao et al., 2021). Tracers are injected into the reservoir and are recovered and detected at an exit point, thus enabling to analyse and simulate the reservoir flow paths and production rates (Weijermars et al., 2017). Further developments in the field of tracer testing saw reactive or ‘smart’ tracers undergo irreversible chemical

changes induced by the conditions inside the reservoir, the detection and analysis of which enables interpretation of reservoir conditions such as pH level or temperature (Nottebohm et al., 2012). However, detection of reactive molecular tracers requires injection of a large amount of the molecules into the reservoir, as recovery rates are low and detection can only occur above a threshold molecular concentration (Chrysikopoulos, 1993). Furthermore, when using smart tracers, correlation between detected chemical transformation of the tracer and the conditions prevalent inside the reservoir may be complicated to perform, as these reactions are based on cumulative processes such as thermal degradation. It is therefore impossible to distinguish for example between long exposure to a relatively low temperature and a short exposure to a more extreme heat (Maier et al., 2015). In addition, interaction of the tracers inside the reservoir due to parameters other than the actual parameters that were intended to govern their responsive behaviour may affect the response of the reactive tracers. For example, the pH value or chemical composition of the reservoir fluids may affect the kinetics of thermal degradation of phenol acetates (Hawkins et al., 2021).

Within this context, we have introduced Reporting Nanoparticles Tracers (RNTs) as a way to realize the potential that lies in smart tracer tests (Rudolph et al., 2020). By coupling threshold mechanisms and irreversible processes, RNTs offer a modular system that has the potential to enhance accuracy, expand the range of measured properties and offers viable solutions to the above mentioned problems, which have thus far limited the application and benefits of using smart tracers. This first report included a proof of concept example of temperature detection under controlled laboratory conditions. The approach is based on nanoparticles that are synthesized with a two-layer architecture, an inner enclosed core and an outer porous shell, each doped with a different fluorescent dye to create a dual emission system. The inner dye is embedded in the particle core structure and cannot leak, providing a stable fluorescence signal that is used as a reference function. In contrast, the dye in the shell, which serves as a reporting function, is not covalently bound to the surface of the particles but is merely contained in the porous shell. The diffusion of the dye out of the particle is prevented by encapsulation with a temperature responsive hull made of paraffin (Fig 1a). The nanoparticles maintain their integrity and structure until a triggering or activation of the messenger nanoparticles occurs, when the melting temperature of the paraffin is exceeded. The hull then melts and the reporting dye in the shell is irreversibly released from the particle (Fig. 1b), thus changing the ratio between the signals of the reporting dye in the shell and the reference dye in the core (report/ref ratio). For an exact detection of the temperature, a sequence of tests can be performed, each using a hull with a different melting point, until an activation event is detected. The RNTs possess a few advantages over alternative tracer testing methods for reservoir characterization: They are based on an irreversible mechanism of operation that is triggered by a sharp threshold and not an accumulative process, which makes it possible to distinguish between the effect of a long exposure of the tracer to moderate conditions and a short exposure to extreme conditions. RNTs possess an inherent reference function, simplifying quantitative analysis of the results. Fluorescence detection and analysis of the result is swift and simple, which enables online tracking of the test and immediate interpretation of its results, and unlike many thermal tracers, both the activated and inactivated forms of the tracer are detectible, thus enabling a more complete understanding of the test results. The RNTs therefore demonstrate a direct, reliable and fast way to determine temperature with a sharp threshold for accurate sensing. Tracer-loaded nanoparticles protect the tracer molecules from direct exposure to the reservoir or aquifer conditions (Alaskar et al., 2015; Mikutis et al., 2018). The RNTs enhance detection sensitivity owing to the fact that they concentrate large numbers of dye molecules in a confined space in comparison to molecular tracers, which are distributed in the entire reservoir volume.

However, for the RNTs to be successfully implemented and deployed, their dispersion needs to be stable enough to enable high transportability and low retention through reservoir media (Nune et al., 2022).

In this work, RNTs are employed in flow-through experiments that emulate flow in a porous aquifer. As a step towards implementation in actual reservoirs, the reporting nanoparticles flow through a quartz sand packed-bed column and their breakthrough curves and recovery rates are compared to those of commonly used conservative molecular tracers, as well as to the values of single-layered fluorescent silica nanoparticles tracers. In addition, effective temperature detection is demonstrated as the fluorescence signals of particles that exceeded the target temperature are distinctly distinguishable from those of unheated RNTs.

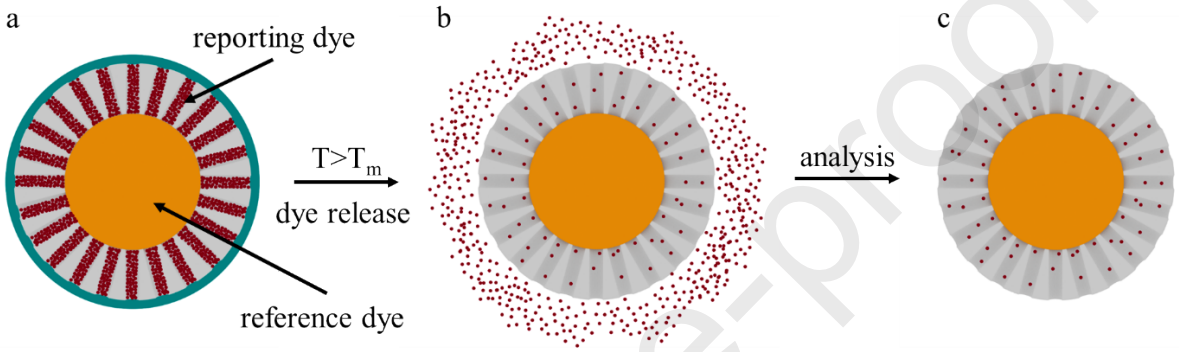

Fig. 1: Schematic representation of the dye release from the shell of the nanoparticles upon exceeding the melting point of the paraffin hull, followed by the analysis of particles with a low report-to-reference (report/ref) ratio after the outer dye had been released.

2. Materials and Methods

Core – shell – hull nanoparticles synthesis:

The synthesis starts with a reverse micro-emulsion reaction (Lian et al., 2004) to create $Ru(bpy)_3^{2+}$-doped silica cores. 7.5 mL cyclohexane (99.5%, VWR Chemicals), 1.77 mL n-hexanol (98%, VWR Chemical), 1.77 mL Triton X-100 (Merck) are mixed and stirred for a minute and then 0.48 mL 20mM Tris(2,2-bipyridyl)dichlororuthenium(II) hexahydrate ($Ru(bpy)_3^{2+}$, 99.95%, Sigma-Aldrich) in millipore H_2O and 0.1 mL tetraethyl orthosilicate (TEOS, 99.0%, Aldrich) are added. The mixture is stirred for 20 minutes and then 0.06 mL 28 - 30% ammonium hydroxide solution (Merck) is added. The micro-emulsion is broken after 24 hours with the addition under stirring of 14 mL of acetone (99.8%, VWR Chemicals). The nanoparticles are collected by centrifugation (6000 rpm, 40 minutes) and are washed in acetone, ethanol (99.9%, VWR Chemicals), 95% v/v ethanol in water mixture and finally deionized water. In the next synthesis step, mesoporous shells are grown around the core nanoparticles based on a synthesis adapted from Liu et al. (2012). A supersaturated 0.2 M cetrimonium bromide (CTAB, 97.0%, Merck) solution is prepared a day in advanced and is kept under constant stirring. The core nanoparticles are sonotrode-dispersed in 3 mL H_2O, to which 10 mL of the 0.2 M CTAB solution is added, followed by stirring for 30 minutes. The particles are then collected by centrifugation (6000 rpm, 30 minutes) and are re-dispersed in 10 mL H_2O (no sonotrode treatment, as this may desorb the CTAB micelles from the surface of the nanoparticles). 0.1 mL of 0.1 M sodium hydroxide (NaOH, 98%, Sigma-Aldrich)

solution in water is added, followed by 3 portions of 60 µL of 20% v/v TEOS in methanol (99.9%, VWR Chemicals) solution over 30 minutes (i.e., a 60 µL portion every 10 minutes, 180 µL in total). After 48 hours under constant stirring, the core-shell nanoparticles are collected by centrifugation (6000 rpm, 40 minutes) and the particles are washed twice in H_2O and once in methanol. The particles are then re-suspended in methanol and the CTAB micelles are extracted by refluxing for 16 hours in a mixture of 120 mL methanol, 2.48 mL H_2O and 1.24 mL hydrochloric acid (HCl, 36.5 – 38%, Fluka) under stirring and heating to 70 °C. The particles are then collected by centrifugation at 6000 rpm, washed with methanol and ethanol and vacuum dried for at least 3 hours before being weighed. Before dye is added it is necessary to remove water molecules that may block the pores so the particles are stored in a water free environment (desiccator purged with dry nitrogen or argon or in a glovebox with H_2O levels lower than 50 ppb), where 17 mg safranin O (95%, Acros Organics) is added to 50 mg of nanoparticles. After 2 hours, dry acetonitrile (99.5%, Merck) is added and the solution is stirred for at least 12 hours. For coating with a paraffin layer, the particles are first hydrophobized in a reaction with 0.375 ml of n-Octadecyltrimethoxysilane (95%, abcr GmbH) that is added outside of the glovebox. The solution is further stirred for at least 12 hours, then the nanoparticles are collected by centrifugation and are washed with acetonitrile and hexane (99%, VWR Chemicals), following which they are vacuum dried. When the nanoparticles are dry the stimuli-responsive layer is added, based on Aznar et al.

, (2011). The particles are resuspended in 40 mL hexane and 375 mg of paraffin is added to the mixture (for example Tetracosane 99%, Dotriacontane 97% or tetratetracontane 99%, all manufactured by Aldrich). The mixture is sonicated for 15 minutes and stirred for 15 minutes, following which the paraffin-coated nanoparticles are collected by centrifugation and dried in vacuum. When the nanoparticless are dry there are re-suspended in water with 1 mg/mL sodium dodecyl sulfate (SDS, 99.0%, Sigma-Aldrich) and undergoes centrifugation – H_2O wash cycles until the residual safranin O is washed away and the supernatant is clear. The particles are then ready for use.

Nanoparticles dispersion: The nanoparticles may be difficult to dissolve along the steps of the above-described multiple-step synthesis, especially after they were vacuum dried or centrifuged. Particle re-suspension was achieved by vortexing and sonication of the reaction vessels or centrifugation tubes. When needed, a sonotrode (IUP200St, Hielscher Ultrasonics) was applied as well. A temperature sensor immersed in the solution regulated this process to ensure that the solution did not exceed the melting point (mp) of the paraffin during sonication. Likewise, longer sonication in sonication baths were performed while maintaining the bath water at room temperature using a circulation thermostat.

Fluorescence spectroscopy: fluorescence spectroscopy was conducted using a Cary Eclipse Fluorescence Spectrophotometer (Agilent Technologies, USA). In-situ heating was conducted by warming the sample holder with a circulation of heating liquid and immersing a temperature probe in the nanoparticle solution. All measurements were performed in 1 cm x 1 cm quartz fluorescence cuvettes.

Dynamic Light Scattering (DLS): DLS measurements were performed using a Particle Sizing Systems (PSS) Nicomp 380 DLS instrument.

Scanning Electron Microscopy (SEM): SEM imaging of the nanoparticles and EDX analysis of the sand grains was performed using a Zeiss LEO 1530 SEM.

Sorption tests: The sorption experiments were performed based on Magal et al. (2008) investigation of sorption properties of fluorescent dye. The quartz sand used in the experiments was repeatedly washed with running water in order to remove suspended solids. The fluid used in the experiments was millipore water that had been mixed with the sand for several hours in order to minimize variations in the pH level of the fluid by the sand, which subsequently could induce changes in the fluorescence signal. The samples consisted of 7 g of the dried sand with 7 mL solutions of uranine (Sigma-Aldrich, 10^{-6} mg/mL), eosin (Apollo Scientific, 97%, 10^{-6} mg/mL), sulforhodamine G (Sigma-Aldrich, 60%, 10^{-7} mg/mL), safranin O (10^{-6} mg/mL), $Ru(bpy)_3^{2+}$ (10^{-5} mg/mL) and a suspension of the RNTs ($5 \cdot 10^{-4}$ g/L). The samples were rocked at 10 RPM for 16 hours with a laboratory shaker (IKA Rocker 3D), after which fluid was collected by centrifugation in order to remove suspended solids. The fluorescence signal was measured and the concentration of the fluorescent dye or the nanoparticles after sorption was determined by using a calibration curve.

3. Results and discussion

3.1 Reporting nanoparticle synthesis, structure and principle of operation

The messenger nanoparticles used in this work have been modified from those reported in Rudolph et al. (2020), as detailed synthesis is described in the Materials and Methods section. For the creation of a stable reference system, silica cores doped with the fluorescent dye Tris-(2,2′-bipyridyl)-ruthenium(II)-chloride ($Ru(bpy)_3^{2+}$) are formed, depicted in Figure 1a as the orange nanoparticle core. During the synthesis, silica precursor molecules condense around $Ru(bpy)_3^{2+}$ dye molecules, resulting in embedded dye molecules in the silica network that do not leak over time. Thus, the stability of the reference signal is ensured. In order to create a reactive reporting function, capable of changing when certain threshold conditions are traversed, a second fluorescent dye is contained in the particle shell. Unlike the reference function of the reporting nanoparticles, irreversibly embedded in the dense silica core, the reference dye is loaded into the shell but is not bound to or trapped inside the nanoparticle. To facilitate this, a mesoporous silica shell is created around the dense silica core and the pores are loaded with the fluorescent dye Safranin O, which functions as the reporting function. The nanoparticle structure is completed with the encapsulation by a paraffin hull, which traps the safranin O molecules within the shell of the nanoparticle (in Figure 1a, the safranin O and porous shell are represented by the red dots inside the grey tubular pores in the shell whereas the hull is the turquois circle surrounding the nanoparticle). The reporting dye can only be released if the melting point (mp) of the paraffin hull is exceeded, thus rendering the paraffin hull permeable to the trapped safranin O molecules (Fig. 1b). The shell and hull of the reporting nanoparticles are hydrophobic, and an amphiphilic surfactant is needed in order to disperse them well in water.

SEM images of the reporting nanoparticles after the initial core growth (average size 44 ± 3 nm) and after the shell growth (average size 72 ± 4 nm) are brought in Supplementary Material Figure 1. The zeta potential of the particles at pH 7 was measured to be -37.2 ± 2.3 mV. Dynamic light scattering (DLS) results (Supplementary Material Fig. 2a) show an

average hydrodynamic diameter of 174.6 ± 29.6 nm concentrated around a single peak, without any sign of particle agglomerations or microscopic silica structures formed in the reaction separately from the nanoparticles.

In comparison to the messenger nanoparticles reported in Rudolph et al. (2020), the adapted RNTs exhibit significantly better dispersion stability in water over time. A certain drawback of this particle type lies in the fact that their shell is smaller and contains less safranin O molecules than the previously reported messenger particles, which generates a smaller reporting signal and a smaller difference in the report/ref ratio when the particles are activated. However, even with lower reporting signal intensity, the nanoparticles can still be detected and analysed at concentrations as low as 1.3 µg/L.

In all experiments reported herein, the hull was made of dotriacontane (melting point 65 – 70 °C). Activation of the reporting nanoparticles took place by heating the solutions to 75 °C.

In addition to the messenger nanoparticles, we have also employed the hydrophilic ($Ru(bpy)_3^{2+}$) doped silica cores (henceforth referred to as core nanoparticles), as an additional tracer. For core nanoparticles, the zeta potential was measured at -25.8 ± 0.4 mV at pH 7 and DLS measurements show an average hydrodynamic diameter of 74.5 ± 10.5 nm, distributed around a narrow intensity peak (Supplementary Material Fig. 2b).

3.2 Experimental setup

The flow through experimental setup is schematically described in Figure 2: A water column (4) is filled with a pump (3) from a tank (2) fed with deionised water (1, conductivity 6.13 MΩ/cm, pH 6.9), so that the column height is always at a constant height of 96 cm above the exit point of the flow system. The water flows through tubes to the bottom of a packed-bed column (7), which is composed of a metal tube filled with quartz sand. The inner side of the tube is lined with quartz sand to prevent direct flow paths along the relatively smooth tube surface. The filling sand is held in place at both edges of the tube with sinter glass plates (pore size 250 µm) and the flow is distributed equally across the cross section of the tube by a star shaped inlet (Supplementary Material Fig. 3). Likewise, to ensure the flow is collected evenly at the end of the column, it is also fitted with a similar star-shaped outlet. The tube leading to the column has two separate points for down-stream injection of particles or additives, one at a controlled and regulated rate with a syringe pump (5) and another for manual injection (6). The flow advances through the column from bottom to top through a flow regulator valve (8) that is used to adjust the flow rate directly into the fluorescence spectrometer (9), where real time spectroscopy is conducted on the current contents of the flow-through cell (measurement frequency of 2 Hz).

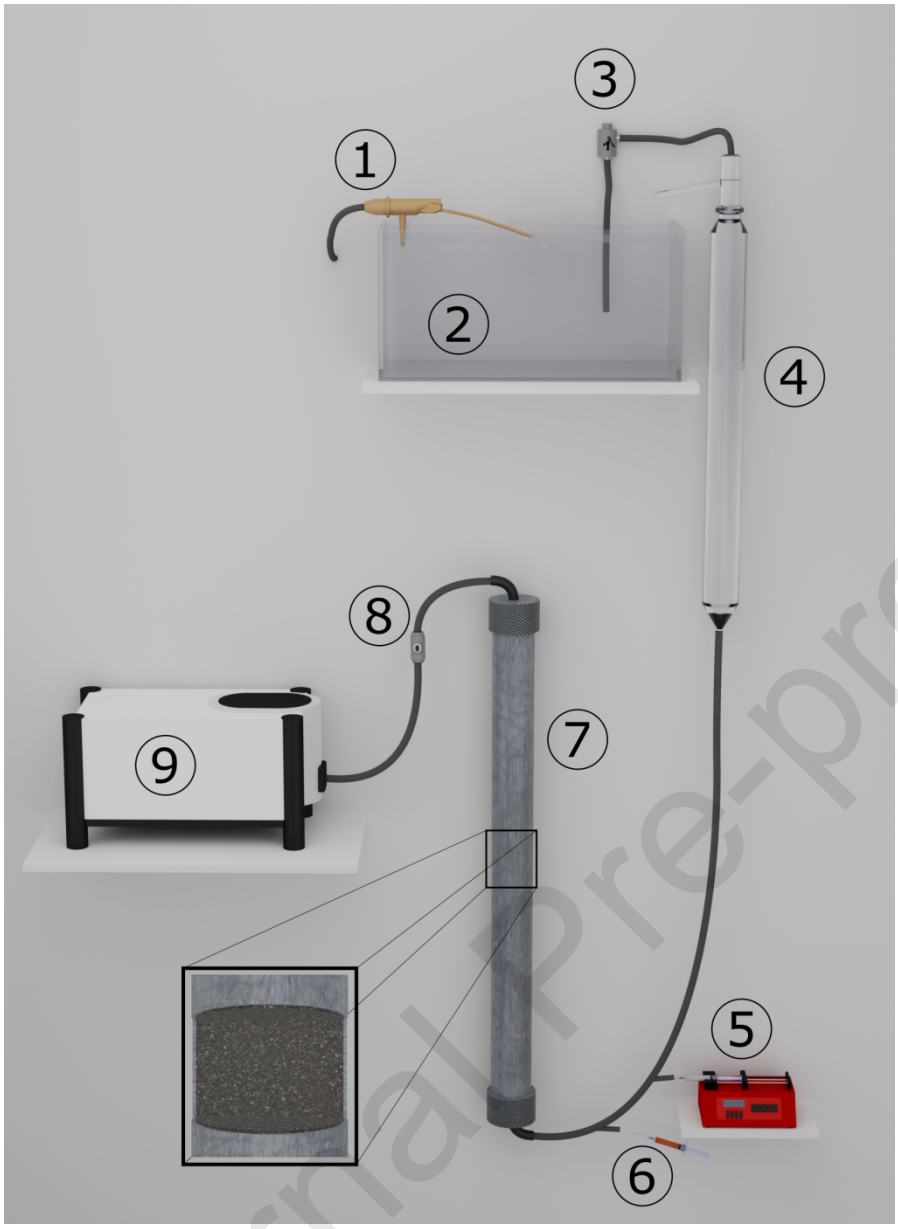

Fig. 2: Schematic representation of the flow-through experimental setup with a water column (4) constantly fed by a pump (3) from a filling tank (2) fed with deionized water (1), in-stream syringe pump controlled (5) and manual (6) sample injection points, packed-bed column (7), valve to adjust flow speed (8) and real-time fluorescence spectroscopy (9) in a flow-through cell.

Two different packed-bed columns were used in the experiments, one 100 cm long and filled with coarse quartz sand (grain size 1.0 – 1.4 mm) and the other 50 cm long and filled with fine quartz sand (grain size 0.1 – 0.6 mm). EDX chemical analysis of molten sand grains is brought in Supplementary Material Table 1. Both metal tubes have an inner diameter of 5.3 cm. Comparison of various flow parameters of both columns is brought in Table 1.

306 Table 1. Calculated parameters of the fine and coarse sand packed-bed columns. Effective
307 porosity is calculated according to (Fetter, 2001).

Parameter	Coarse sand column	Fine sand column
Grain size	1.0 – 1.4 mm	0.1 – 0.6 mm
Tube inner diameter	5.3 cm	5.3 cm
Tube length	100 cm	50 cm
Flow rate	4.05 mL/s	2.02 mL/s
Hydraulic gradient	0.87 m	2.74 m
Cross section area	$2.21 \cdot 10^{-3}$ m^2	$2.21 \cdot 10^{-3}$ m^2
Effective porosity (Fetter, 2001)	28%	26%
Flow velocity	$6.48 \cdot 10^{-3}$ m/s	$3.49 \cdot 10^{-3}$ m/s
Hydraulic conductivity	$2.08 \cdot 10^{-3}$ m/s	$3.31 \cdot 10^{-4}$ m/s
Permeability	$2.13 \cdot 10^{-10}$ m^2	$3.39 \cdot 10^{-11}$ m^2
Diffusion coefficient	$6.12 \cdot 10^{-12}$ m^2/s	$6.12 \cdot 10^{-12}$ m^2/s
Peclet number	$2.96 \cdot 10^{8}$	$7.40 \cdot 10^{7}$

308

309

310 3.3 Flow experiments

311 Flow experiments were conducted with the above described packed-bed column –
312 fluorescence spectroscopy setup to examine the ability of the reporting nanoparticles to flow
313 through a simulated reservoir, the feasibility of temperature detection by distinguishing
314 unheated and heated nanoparticles and quantifying the amount of particles recovered after
315 the particles passed through the column. These results were compared to similar tests
316 performed with solutions of the widely-used conservative molecular tracers uranine, eosin

and sulforhodamine G. Eventually, recovery experiments were also conducted using thermal fluid collected from a natural hot spring (vide infra).

Breakthrough curves were obtained by injecting molecular tracer or nanoparticle solutions downstream through a septum, 16 cm before the fluids enter the packed-bed column. The 1 mL injections were performed manually in one abrupt movement, so that each measurement has virtually an identical starting point of a sharp tracer concentration spike, which then propagates differently throughout the column volume as a result of different interaction with the sand and the carrying fluids. Due to the injection method using a syringe, the injected volume is assumed with an error of 5%.

3.3.1 Molecular Tracers and nanoparticles in coarse and fine sand columns

The breakthrough curves in coarse sand column of 1 mL of the molecular tracers solutions of uranine (10^{-3} mg/mL), eosin (10^{-2} mg/mL), and sulforhodamine G ($5 \cdot 10^{-3}$ mg/mL) are shown in Figure 3a (left). For comparison purposes, two nanoparticle suspensions were used in the flow-through tests: the $Ru(bpy)_3^{2+}$-doped core nanoparticles (the inner layer of the RNT, containing the reference dye) and the RNTs. The main difference between the two nanoparticles is that the core particles are hydrophilic and are naturally dispersed in water whereas the RNTs have an hydrophobic outer layer and its dispersion in water therefore requires a surfactant (the anionic SDS in this case). The breakthrough curves of the core nanoparticles and the RNTs are shown in Figure 3a (right). It is worth noting that both dyes used in the reporting nanoparticles, i.e. $Ru(bpy)_3^{2+}$ and safranin O, showed significant sorption on the column matrix to the extent that dye solutions, even at concentrations as high as 2 mg/mL, resulted in no clear breakthrough curves but rather miniscule amounts of dye exiting the column steadily over days. It is therefore safe to say that detection of $Ru(bpy)_3^{2+}$ and safranin O signals can be solely attributed to detection of nanoparticles and not to free dye molecules that are the result of dye release or particle disintegration during flow through the column.

Comparison of the time of first exit (T_{min}), time of maximal concentration (T_{peak}), maximum breakthrough velocity (V_{max}), peak velocity (V_{peak}), the dispersion coefficient (D_L, calculated with STANMOD software), retardation factor (R, calculated with STANMOD software) and the calculated recovery rates of the different tracers and nanoparticles is brought in Table 2.

Amongst the molecular tracers, uranine, which is widely used as a conservative tracer (Luhmann et al., 2012), shows a maximum breakthrough velocity V_{max} of $6.49 \cdot 10^{-3}$ m/s, which is very close to the theoretically calculated flow velocity in the system of $6.72 \cdot 10^{-3}$ m/s (calculated according to Darcy's law (Whitaker, 1986)). In contrast, eosin and sulforhodamine G show a much stronger retardation and have increased dispersion coefficient D_L values of 135 and 234 cm^2/min, respectively.

In comparison to the molecular tracers, the core and reporting nanoparticles show reduced dispersion and earlier arrival time. The breakthrough velocity values of $6.62 \cdot 10^{-3}$ m/s (core nanoparticles) and $6.74 \cdot 10^{-3}$ m/s (RNTs) are above the theoretically calculated flow velocity, as a result of the tendency of the colloidal tracers to prefer low tortuous flow paths through a porous medium (Bradford et al., 2002). In addition, the nanoparticles exhibit a smaller dispersion coefficient (17 and 20 cm^2/min for core and reporting nanoparticles, respectively) and retardation factor (1.3 for core nanoparticles and 1.4 for RNTs in comparison to 1.8 for uranine). In contrast to the nanoparticles, the breakthrough curves of molecular tracers show long tailings as the injected tracers end up in deadzones with lower flow velocity, from which only the molecular tracers diffuse out over time. Although the size of the nanoparticles leads to loss due to filtration processes and sedimentation (Chen and Kibbey, 2009), the recovery

rates are nevertheless on par with conservative molecular tracers: 81.0% of the RNTs and 71.8% of the core nanoparticles were recovered in comparison to 95.0% of the uranine, 49.6% of the sulforhodamine G and just 16.0% of the eosin. This in part can be attributed to the weak electrostatic interaction of the RNTs with the quartz sand in the column, as has been corroborated by performing sorption tests. The sorption of fluorescent dyes is dominated by electrostatic interactions in the absence of extreme pH values, which are in turn strongly dependent on the type and number of functional groups in the tracer molecules (Kasnavia et al., 1999).

To investigate the sorption behaviour of the reporting and the molecular tracers, a series of sorption experiments were performed, in accordance with similar experiments reported in Magal et al. (2008). Samples of the coarse quartz sand were repeatedly washed with tap water in order to remove suspended solids and to produce a comparable grain composition to the sand contained in the column. Samples of dried sand, uranine, eosin and sulforhodamine G, as well as the dyes of the reporting nanoparticles safranin O and $Ru(bpy)_3^{2+}$, and a suspension of the reporting nanoparticles was prepared as described in the Materials and Methods section. The solutions were prepared in varying concentrations as a result of different fluorescence intensities of the dyes, with the aim of obtaining strong fluorescence intensities for each solution to minimize measurement error. The sand/tracer mixtures were lightly shaken for 16 hours and then centrifuged (apart from the nanoparticles solution). The fluorescence intensity of the solutions was compared before and after mixing with sand and the adsorbed fraction was determined based on concentration curves. The results of the sorption experiments are shown in Figure 3c. The reporting nanoparticle tracers show only 6% loss of concentration in solution due to sorption, in comparison to strong sorption in the cases of safranin O 78% and $Ru(bpy)^{2+}_3$ 99%. Uranine (16%), eosin (27%) and sulforhodamine G (23%) show intermediate values, which are in agreement with the obtained breakthrough curves. The lower sorption of the RNTs in comparison to uranine even though uranine exhibits a higher recovery rate demonstrates that the recovery rate is the result of the interplay of multiple parameters. While the attractive forces of the tracer-fluid-rock interaction are lower in the case of RNTs than for the uranine molecules, the size of the nanoparticles results in higher loss due to effects such as filtration.

Table 2. Tracer and nanoparticle flow parameters calculated from breakthrough curves of flow experiments through a coarse sand packed-bed column. The maximum breakthrough velocity (V_{max}) and peak velocity (V_{peak}) were calculated using STANMOD software (Toride et al., 1995) for uranine, core and reporting nanoparticles and the C_{peak} modelling method (Małoszewski and Zuber, 1985) for eosin and sulforhodamine G.

	T_{min} (s)	T_{peak} (s)	V_{max} (10^{-3} m/s)	V_{peak} (10^{-3} m/s)	D_L (cm^2/min)	R	Recovery rate (%)

Uranine	154	243	6.49	4.11	89	1.8	95.0±4.8
Eosin	201	403	4.97	2.48	135	N/A	16.0±0.8
Sulforhodamine G	156	1200	6.41	0.83	234	N/A	49.6±2.5
Core NPs	151	227	6.62	4.40	17	1.3	71.8±3.6
Reporting NPs	148	220	6.74	4.53	20	1.4	81.0±4.0

405

406 In addition to the experiments with the coarse sand, flow experiments were also performed on a
407 50 cm fine sand column, in which a flow rate of 2 mL/s was measured. Figure 3b (left) shows
408 the breakthrough curves of uranine, eosin and sulforhodamine G. While uranine and
409 sulforhodamine G show a very similar behavior to the experiments with coarse sand, eosin
410 proved to be unsuitable for fine sand test system. The tendency for strong retention observed in
411 coarse sand was even more pronounced in the case of fine-grained sand. Even after 3 hours of
412 flow, a tailing with 40% of the maximal peak intensity was observed. In addition, the intensity of
413 the tailing increased again after 120 minutes of flow, displaying an overlap of at least two flow
414 paths. The tracer recovery rates at the end of the respective measurements were 89 ± 4.4% for
415 uranine after 70 minutes, 16 ± 0.8% for eosin after 170 minutes, and 9 ± 0.5% for
416 sulforhodamine G after 180 minutes. Core nanoparticles and the RNTs were tested in the fine
417 sand column as well (Fig. 3b, right).

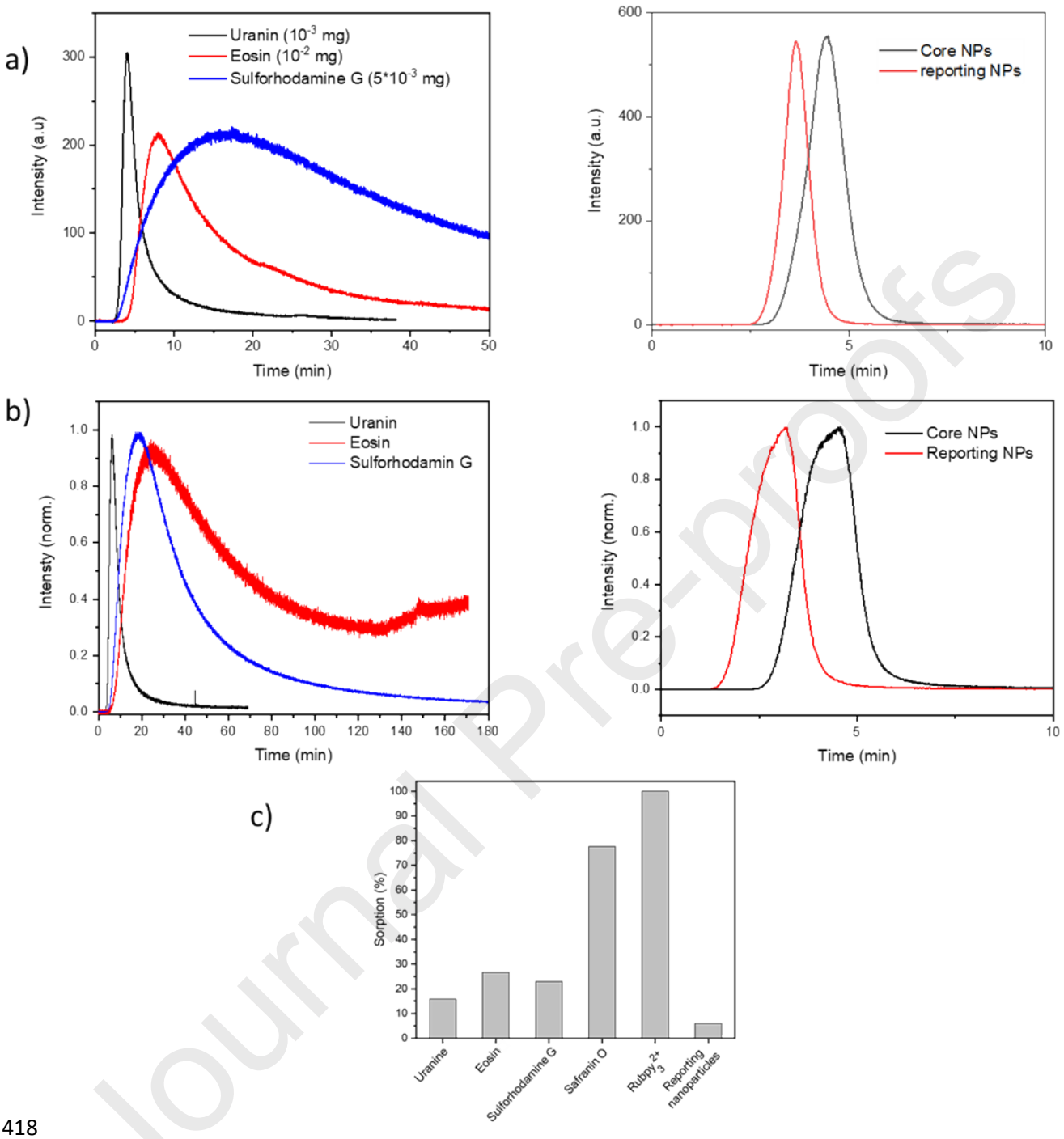

418

419

420 Fig. 3: a) Breakthrough curves of molecular tracers (left) and nanoparticles (right) through a
421 coarse sand packed-bed column. b) Breakthrough curves of molecular tracers (left) and
422 nanoparticles (right) through a fine sand packed-bed column. c) Sorption rate of molecular
423 tracers and reporting nanoparticles with coarse quartz sand.

424

425 Since the fine sand has a larger surface area and smaller pore spaces, the probability of
426 particle-sand interactions increases, which is exacerbated by the slower flow speed. When

observing the nanoparticle breakthrough curves, it is evident that the breakthrough speed of the larger RNTs is significantly faster than that of the smaller core nanoparticles. This indicates a faster flow path through the porous matrix and/or a significantly reduced adsorption. Despite this difference, the total recovery rates of the reporting and core nanoparticles were similar, calculated to be 42 ± 2.1% and 43 ± 2.2%, respectively. The lower recovery rates compared to those obtained in the coarse sand column show particle loss due to reduced effective pore size, leading to enhanced filtraion and increased sedimentation with lower flow rate, owing to increased surface interaction. Table 3 compares the flow parameters of the molecular tracers and nanoparticles in the fine sand column.

Table 3. Tracer and nanoparticle flow parameters calculated from breakthrough curves of flow experiments through a fine sand packed-bed column. The maximum breakthrough velocity (V_{max}) and peak velocity (V_{peak}) were calculated using STANMOD software (Toride et al., 1995) for uranine, core and reporting nanoparticles and the C_{peak} modelling method (Małoszewski and Zuber, 1985) for eosin and sulforhodamine G

	T_{min} (s)	T_{peak} (s)	V_{max} (10^{-3} m/s)	V_{peak} (10^{-3} m/s)	D_L (cm^2/min)	R	Recovery rate (%)
Uranine	186	360	2.68	1.39	45	2.8	89.1±4.4
Eosin	305	1505	1.63	0.33	N/A	N/A	16.2±0.8
Sulforhodamine G	266	1110	1.88	0.45	N/A	N/A	9.1±0.5
Core NPs	142	277	3.52	1.80	13	1.8	43.0±2.2
Reporting NPs	86	187	5.81	2.68	22	1.3	42.0±2.1

3.3.2 Flow experiments with thermal spring water

Since the future field application of the reporting nanoparticles is expected to be in fluids with increased salinity, in addition to the experiments with deionized water, flow experiments through coarse sand with water from a thermal spring in Baden-Baden were carried out. The water originates from a freely accessible source (coordinates: 48.765303619511975, 8.241837662309175) and has a pH-value of 7.04, a temperature of 60°C at the surface, a salinity of about 3 g/L and a conductivity of 4.38 µS/cm (see Supplementary Material Table 2 for chemical analysis of the thermal water). The values are similar to those of the nearby Fettquelle spring, which is well characterized (Sanjuan et al., 2016) and has comparable

TDS values to those found in intermediate-temperature geothermal fluids (90-150 °C) in the USA (Gude, 2018).

Under these conditions, the reporting nanoparticles were recovered at 89.1 ± 7.0% of the injected amount, higher than the 81.0% value obtained with deionized water as fluid. In both flow experiments using deionized water and thermal spring water, the report/ref ratio was equal at 0.17. This indicates that in both cases the measured signals only emanate from the reporting nanoparticles and not from free dye molecules in the column or fluorescence of other sources contained in the background fluid. This is an unexpected result, as according to the DLVO theory, an increase in electrolyte concentration in the fluid reduces the repulsive electrostatic forces between the particles (particle-particle interaction) and between the particles and the porous matrix. Reduced repulsion, in turn, weakens the effective zeta potential and results in increased agglomeration, retention and deposition rates. A possible explanation may emanate from the hydrophobic shell of the particles and the amphiphilic surfactant molecules used for the dispersion of the nanoparticles in water and their interaction with the surrounding matrix, which may behave differently from the basic case described in the DLVO theory. This possibility seems reasonable especially in light of the fact that the recovery rate of core nanoparticles, which are not suspended using SDS, is only 33.7% in spring water in comparison to 71,8% in deionized water. Another possibility would be a weakening of attractive forces within the sand matrix by the thermal spring water due to shielding of the charge of the quartz sand grains by ions from the solution.

3.3.3 Reporting nanoparticles and temperature detection

With the characterization of the flow behaviour of prevalent molecular tracers as a basis for comparison, the following experiments tested the flow characteristics of reporting nanoparticles. The reporting nanoparticles were injected in their initial, unreacted state (unheated) as well as in their activated state (heated), after the temperature threshold had been crossed and had induced dye release from shell. Figure 4a shows the outcome of heating the reporting nanoparticles above the threshold temperature. The initial fluorescence signal of the unheated reporting nanoparticles (grey curve) was obtained by sweeping the excitation wavelength and measuring the resulting emission at the 612 nm wavelength. The spectrum is composed of a peak for the $Ru(bpy)_3^{2+}$ dye embedded in its core (reference function) at 452 nm and a peak for the safranin O in the shell (reporting function) at 530 nm. After deconvolution of the slightly overlapping indicators, the resulting intensity ratio between the reporting and the reference signals (report/ref ratio) was calculated to be 0.58. After heating, the safranin O dye in the shell was released into the solution, which resulted in less spatial confinement-induced fluorescence quenching and brought about a significant increase in the fluorescence intensity of the reporting dye. This could be clearly distinguished both by colour change of the solution (Fig. 4a, right) and by fluorescence spectroscopy (red curve) with an over 6-fold increase in the report/ref ratio to 3.54. In flow experiments, 1 mL of 0.5 mg/mL unheated and heated reporting nanoparticles solutions were introduced separately into the packed-bed coarse sand column, to examine whether they could be detected and whether activated nanoparticles were distinguishable from those that did not exceed the threshold temperature. Figure 4b shows the real time measurement of fluorescence signals of the RNTs (reference signal orange curves and reporting signal dark red curves). The heated sample shows an increase in the reporting signal intensity and consequently has a higher report/ref ratio. The report/ref ratio changes from 0.62 for the unheated sample to 0.93 for the heated one. Thus, temperature detection by differentiating heated from unheated RNTs could be unambiguously achieved. The fact that release of the reporting dye causes an increase in the report/ref ratio may seem counterintuitive, yet a certain amount of dye remains trapped in the shell and these remnants now yield a much stronger fluorescence signal as the decrease in dye molecule concentration significantly

diminishes fluorescence quenching of densely packed molecules (Andreiuk et al., 2019). It should be pointed out that an increase in the reporting signal as a result of free safranin O molecules that had been released from the particles and flows separately through the column can be ruled out as unlikely and negligible, since apart from the strong adsorption of the dye in the column, the reporting intensity perfectly coincides with the reference signal emanating from the particles' core.

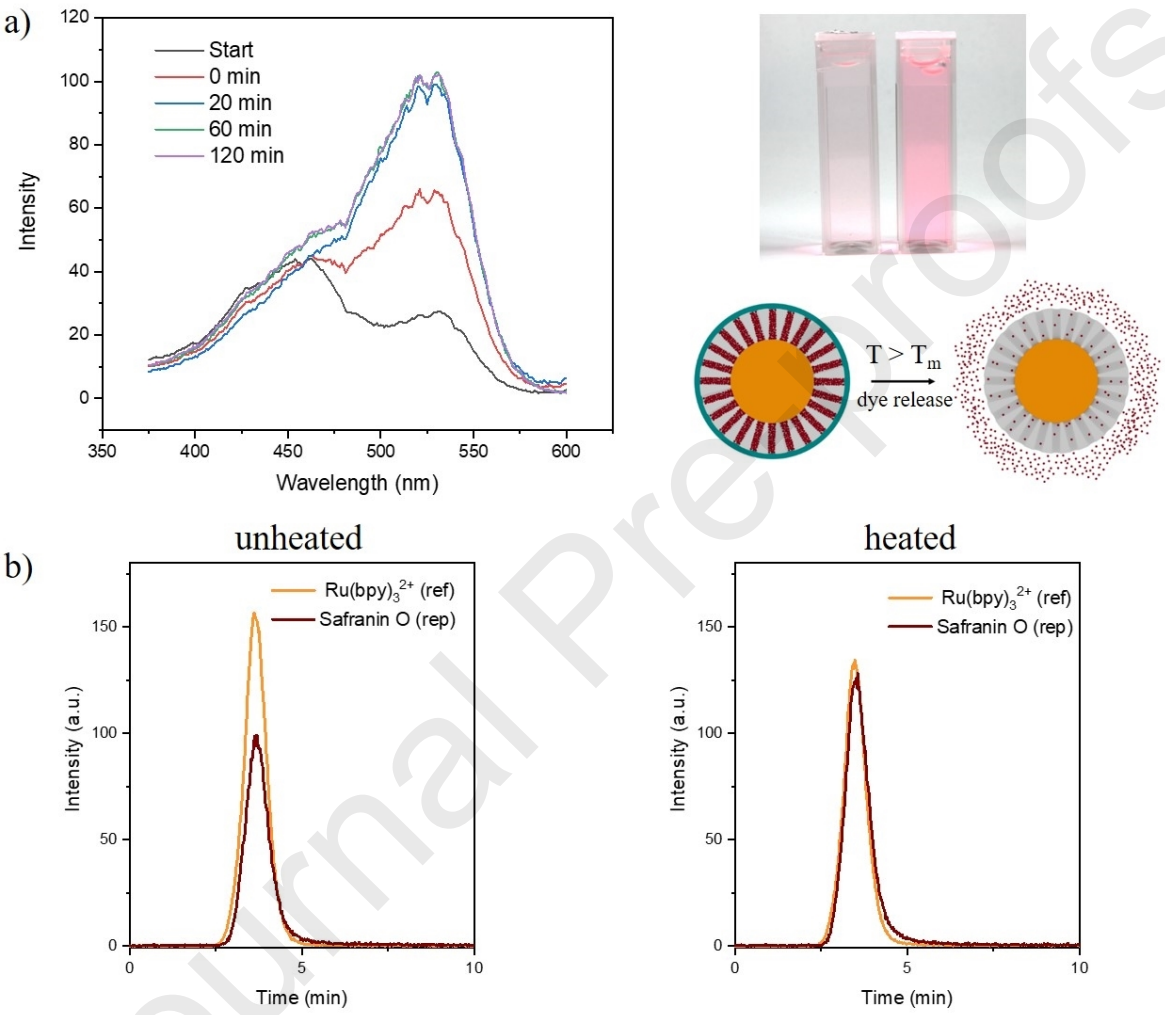

Fig. 4: **(a)** Fluorescence spectroscopy (left) and image (right) of unheated (grey curve, left cuvette) and heated (right cuvette) RNT solution with the corresponding schematic depiction of the state of the RNTs. **(b)** Real-time flow-through fluorescence spectroscopy of unheated (left) and heated (right) RNT solutions, after flowing through the packed-bed column.

4. Conclusions

With its high sensitivity and accuracy of detection, the herein discussed approach to tracer testing of aquifers and reservoirs based on Reporting Nanoparticle Tracers bears a promise to advance and improve characterization and monitoring capabilities. However, the road

from a theoretical approach to a method that can be successfully and practically applied in the field is not trivial, and requires stepwise tests with increasing levels of complexity.

The initial experimental results confirmed that the RNTs function well under controlled laboratory conditions, being activated irreversibly by external stimuli with sharp threshold and carry a reporting and a reference function that enables unequivocal detection of the external stimuli event. This report takes the next step to demonstrate the capability of the RNTs to flow through a simulated subsurface medium operating with a thermal fluid.

Indeed, the flow experiments presented in this report show that the tested RNTs can successfully be carried by thermal fluid and flow through porous medium at flow and recovery rates comparable to and in some cases surpassing those of the most prevalent conservative molecular tracers. Thus, the nanoparticles elude possible hurdles such as irreversible adsorption on the rock surface (both before and after melting of the paraffin hull), agglomeration or clustering in the thermal fluid or leak of the paraffin hull under the diverse and uncontrollable chemical ambience of the simulated system.

In addition, the advantage of modularity of the RNT design and synthesis is demonstrated. While their principle of operation remains identical, the adapted reporting nanoparticles were created with the purpose of reducing possible agglomeration and increasing the particle recovery rate. The adapted synthesis procedure yielded nanoparticles with better size distribution that are better dispersed in solution, which in turn yielded a higher recovery rate in the flow experiments. Before injection, the current synthesis of the reporting nanoparticles enables dispersion with different surfactants to ensure the best solubility in different natural fluids and to adapt to the conditions in each specific aquifer or reservoir. The experiments with thermal spring water demonstrate how far the choice of an adequate surfactant can affect the results, with the surfactant-coated RNTs exhibiting more than double the recovery rate of that of the bare core particles in the saline fluid.

More generally, looking toward future application in complex natural systems, it should be pointed out that RNT parameters such as particle size, charge and surface functionality, as well as external elements such as surfactants and additives, can all be adapted to adjust the nanoparticles to the challenges of the specific conditions. Hence, a wide range of tools are available to make these reporting nanoparticles a viable and practical approach to reservoir characterization.

Abbreviations

RNTs - Reporting Nanoparticle Tracers

DLS - Dynamic Light Scattering

SEM - Scanning Electron Microscopy

EDX - Energy-Dispersive X-ray Spectroscopy

SDS - Sodium Dodecyl Sulfate

TDS - Total Dissolved Solids

mp – Melting Point

Acknowledgements

This study is part of the subtopic “Geoenergy” in the program “MTET—Materials and Technologies for the Energy Transition” of the Helmholtz Association.

References

Alaskar, M., Ames, M., Liu, C., Li, K., Horne, R., 2015. Temperature nanotracers for fractured reservoirs characterization. Journal of Petroleum Science and Engineering 127, 212-228.

Andreiuk, B., Reisch, A., Bernhardt, E., Klymchenko, A.S., 2019. Fighting Aggregation-Caused Quenching and Leakage of Dyes in Fluorescent Polymer Nanoparticles: Universal Role of Counterion. Chemistry – An Asian Journal 14(6), 836-846.

Aznar, E., Mondragón, L., Ros-Lis, J.V., Sancenón, F., Marcos, M.D., Martínez-Máñez, R., Soto, J., Pérez-Payá, E., Amorós, P., 2011. Finely Tuned Temperature-Controlled Cargo Release Using Paraffin-Capped Mesoporous Silica Nanoparticles. Angewandte Chemie International Edition 50(47), 11172-11175.

Bradford, S.A., Yates, S.R., Bettahar, M., Simunek, J., 2002. Physical factors affecting the transport and fate of colloids in saturated porous media. Water Resources Research 38(12), 63-61-63-12.

Chen, L., Kibbey, T.C., 2009. Transport of nanomaterials in unsaturated porous media.

Chrysikopoulos, C.V., 1993. Artificial tracers for geothermal reservoir studies. Environmental Geology 22(1), 60-70.

Fetter, C.W., 2001. Applied hydrogeology. Prentice Hall, Upper Saddle River, N.J.

Fronzi, D., Di Curzio, D., Rusi, S., Valigi, D., Tazioli, A., 2020. Comparison between Periodic Tracer Tests and Time-Series Analysis to Assess Mid- and Long-Term Recharge Model Changes Due to Multiple Strong Seismic Events in Carbonate Aquifers. Water 12(11), 3073.

Gasser, G., Rona, M., Voloshenko, A., Shelkov, R., Tal, N., Pankratov, I., Elhanany, S., Lev, O., 2010. Quantitative Evaluation of Tracers for Quantification of Wastewater Contamination of Potable Water Sources. Environmental Science & Technology 44(10), 3919-3925.

Gude, V.G., 2018. Chapter 4 - Geothermal Source for Water Desalination—Challenges and Opportunities, in: Gude, V.G. (Ed.) Renewable Energy Powered Desalination Handbook. Butterworth-Heinemann, pp. 141-176.

Hawkins, A.J., Bender, J.T., Grooms, R.D., Schissel, C.J., Tester, J.W., 2021. Temperature-responsive smart tracers for field-measurement of inter-well thermal evolution: Heterogeneous kinetics and field demonstration. Geothermics 92, 102046.

Hsieh, P.-S., Lin, C.-K., Chang, Y.-T., Lu, H.-Y., Yang, T.F., 2021. The GTFSampler: A new downhole equipment for geothermal fluid sampling and its testing results in the Chingshiu geothermal field, Ilan, Taiwan. Geothermics 94, 102077.

Ju, Y., Massoudieh, A., Kaown, D., Yoon, Y.-Y., Lee, K.-K., 2020. Characterization of flow dynamics around highly-utilized agricultural wells in a fractured-rock aquifer: Assessment of uncertainties lying on groundwater age-dating. Journal of Hydrology 586, 124885.

Kasnavia, T., Vu, D., Sabatini, D.A., 1999. Fluorescent Dye and Media Properties Affecting Sorption and Tracer Selection. Groundwater 37(3), 376-381.

Kruszewski, M., Wittig, V., 2018. Review of failure modes in supercritical geothermal drilling projects. Geothermal Energy 6(1), 28.

Lian, W., Litherland, S.A., Badrane, H., Tan, W., Wu, D., Baker, H.V., Gulig, P.A., Lim, D.V., Jin, S., 2004. Ultrasensitive detection of biomolecules with fluorescent dye-doped nanoparticles. Analytical biochemistry 334(1), 135-144.

Liu, J., Bu, W., Zhang, S., Chen, F., Xing, H., Pan, L., Zhou, L., Peng, W., Shi, J., 2012. Controlled synthesis of uniform and monodisperse upconversion core/mesoporous silica shell nanocomposites for bimodal imaging. Chemistry–A European Journal 18(8), 2335-2341.

Luhmann, A.J., Covington, M.D., Alexander, S.C., Chai, S.Y., Schwartz, B.F., Groten, J.T., Alexander, E.C., 2012. Comparing conservative and nonconservative tracers in karst and using them to estimate flow path geometry. Journal of Hydrology 448-449, 201-211.

Magal, E., Weisbrod, N., Yakirevich, A., Yechieli, Y., 2008. The use of fluorescent dyes as tracers in highly saline groundwater. Journal of Hydrology 358(1), 124-133.

Maier, F., Schaffer, M., Licha, T., 2015. Temperature determination using thermo-sensitive tracers: Experimental validation in an isothermal column heat exchanger. Geothermics 53, 533-539.

Małoszewski, P., Zuber, A., 1985. On the theory of tracer experiments in fissured rocks with a porous matrix. Journal of Hydrology 79(3-4), 333-358.

Mikutis, G., Deuber, C.A., Schmid, L., Kittilä, A., Lobsiger, N., Puddu, M., Asgeirsson, D.O., Grass, R.N., Saar, M.O., Stark, W.J., 2018. Silica-encapsulated DNA-based tracers for aquifer characterization. Environmental science & technology 52(21), 12142-12152.

Nottebohm, M., Licha, T., Sauter, M., 2012. Tracer design for tracking thermal fronts in geothermal reservoirs. Geothermics 43, 37-44.

Nune, S.K., Miller, Q.R.S., Schaef, H.T., Jian, T., Song, M., Li, D., Shuttanandan, V., McGrail, B.P., 2022. Transport of polymer-coated metal–organic framework nanoparticles in porous media. Scientific Reports 12(1), 13962.

Olasolo, P., Juárez, M.C., Morales, M.P., D´Amico, S., Liarte, I.A., 2016. Enhanced geothermal systems (EGS): A review. Renewable and Sustainable Energy Reviews 56, 133-144.

Rudolph, B., Berson, J., Held, S., Nitschke, F., Wenzel, F., Kohl, T., Schimmel, T., 2020b. Development of thermo-reporting nanoparticles for accurate sensing of geothermal reservoir conditions. Scientific reports 10(1), 1-7.

Salley, K.A., Stotler, R.L., Johnson, W.C., Burt, D.J., Hirmas, D.R., Fiefeld, K., Bowen, M.W., Kastens, J.H., Ryuh, Y.-G., 2022. Hydrology of a Hydroperiod: Assessing Recharge to the High Plains Aquifer Through a Playa in Western Kansas. Journal of Hydrology, 128141.

Sanjuan, B., Millot, R., Innocent, C., Dezayes, C., Scheiber, J., Brach, M., 2016. Major geochemical characteristics of geothermal brines from the Upper Rhine Graben granitic basement with constraints on temperature and circulation. Chemical Geology 428, 27-47.

Sarris, T.S., Close, M., Abraham, P., 2018. Using solute and heat tracers for aquifer characterization in a strongly heterogeneous alluvial aquifer. Journal of hydrology 558, 55-71.

Toride, N., Leij, F., Van Genuchten, M.T., 1995. The CXTFIT code for estimating transport parameters from laboratory or filed tracer experiments. US Salinity Laboratory Riverside, CA.

Weijermars, R., Zuo, L., Warren, I., 2017. Modeling Reservoir Circulation and Economic Performance of the Neal Hot Springs Geothermal Power Plant (Oregon, U.S.): An Integrated Case Study. Geothermics 70, 155-172.

Whitaker, S., 1986. Flow in porous media I: A theoretical derivation of Darcy's law. Transport in Porous Media 1(1), 3-25.

Witter, J.B., Trainor-Guitton, W.J., Siler, D.L., 2019. Uncertainty and risk evaluation during the exploration stage of geothermal development: A review. Geothermics 78, 233-242.

Zhao, Z., Dou, Z., Liu, G., Chen, S., Tan, X., 2021. Equivalent flow channel model for doublets in heterogeneous porous geothermal reservoirs. Renewable Energy 172, 100-111.

Parameter	**Coarse sand column**	**Fine sand column**
Grain size	1.0 – 1.4 mm	0.1 – 0.6 mm
Tube inner diameter	5.3 cm	5.3 cm
Tube length	100 cm	50 cm
Flow rate	4.05 mL/s	2.02 mL/s
Hydraulic gradient	0.87 m	2.74 m
Cross section area	$2.21 \cdot 10^{-3}$ m^2	$2.21 \cdot 10^{-3}$ m^2
Effective porosity (Fetter, 2001)	28%	26%

Flow velocity	$6.48 \cdot 10^{-3}$ m/s	$3.49 \cdot 10^{-3}$ m/s
Hydraulic conductivity	$2.08 \cdot 10^{-3}$ m/s	$3.31 \cdot 10^{-4}$ m/s
Permeability	$2.13 \cdot 10^{-10}$ m^2	$3.39 \cdot 10^{-11}$ m^2
Diffusion coefficient	$6.12 \cdot 10^{-12}$ m^2/s	$6.12 \cdot 10^{-12}$ m^2/s
Peclet number	$2.96 \cdot 10^{8}$	$7.40 \cdot 10^{7}$

661

662

	T_{min} (s)	**T_{peak} (s)**	**V_{max} (10^{-3} m/s)**	**V_{peak} (10^{-3} m/s)**	**D_L (cm^2/min)**	**R**	**Recovery rate (%)**
Uranine	154	243	6.49	4.11	89	1.8	95.0±4.8
Eosin	201	403	4.97	2.48	135	N/A	16.0±0.8
Sulforhodamine G	156	1200	6.41	0.83	234	N/A	49.6±2.5
Core NPs	151	227	6.62	4.40	17	1.3	71.8±3.6
Reporting NPs	148	220	6.74	4.53	20	1.4	81.0±4.0

663

664

	T_{min} (s)	**T_{peak} (s)**	**V_{max} (10^{-3} m/s)**	**V_{peak} (10^{-3} m/s)**	**D_L (cm^2/min)**	**R**	**Recovery rate (%)**
Uranine	186	360	2.68	1.39	45	2.8	89.1±4.4

Eosin	305	1505	1.63	0.33	N/A	N/A	16.2±0.8
Sulforhodamine G	266	1110	1.88	0.45	N/A	N/A	9.1±0.5
Core NPs	142	277	3.52	1.80	13	1.8	43.0±2.2
Reporting NPs	86	187	5.81	2.68	22	1.3	42.0±2.1

665

666

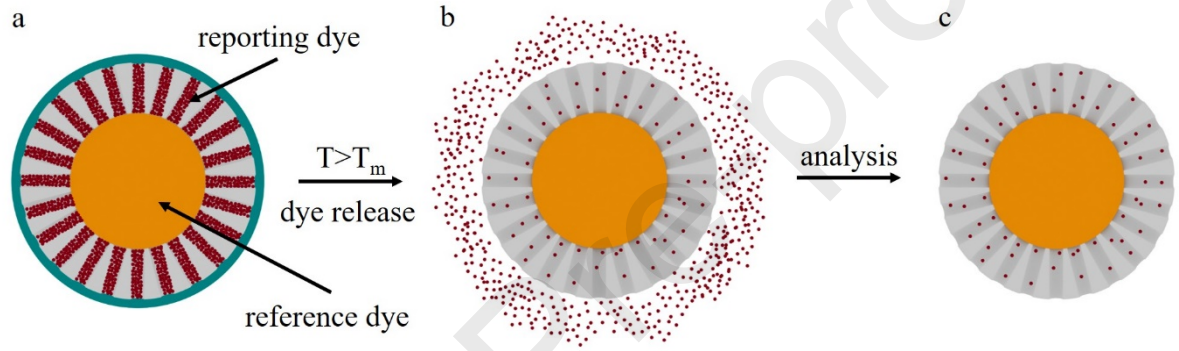

667

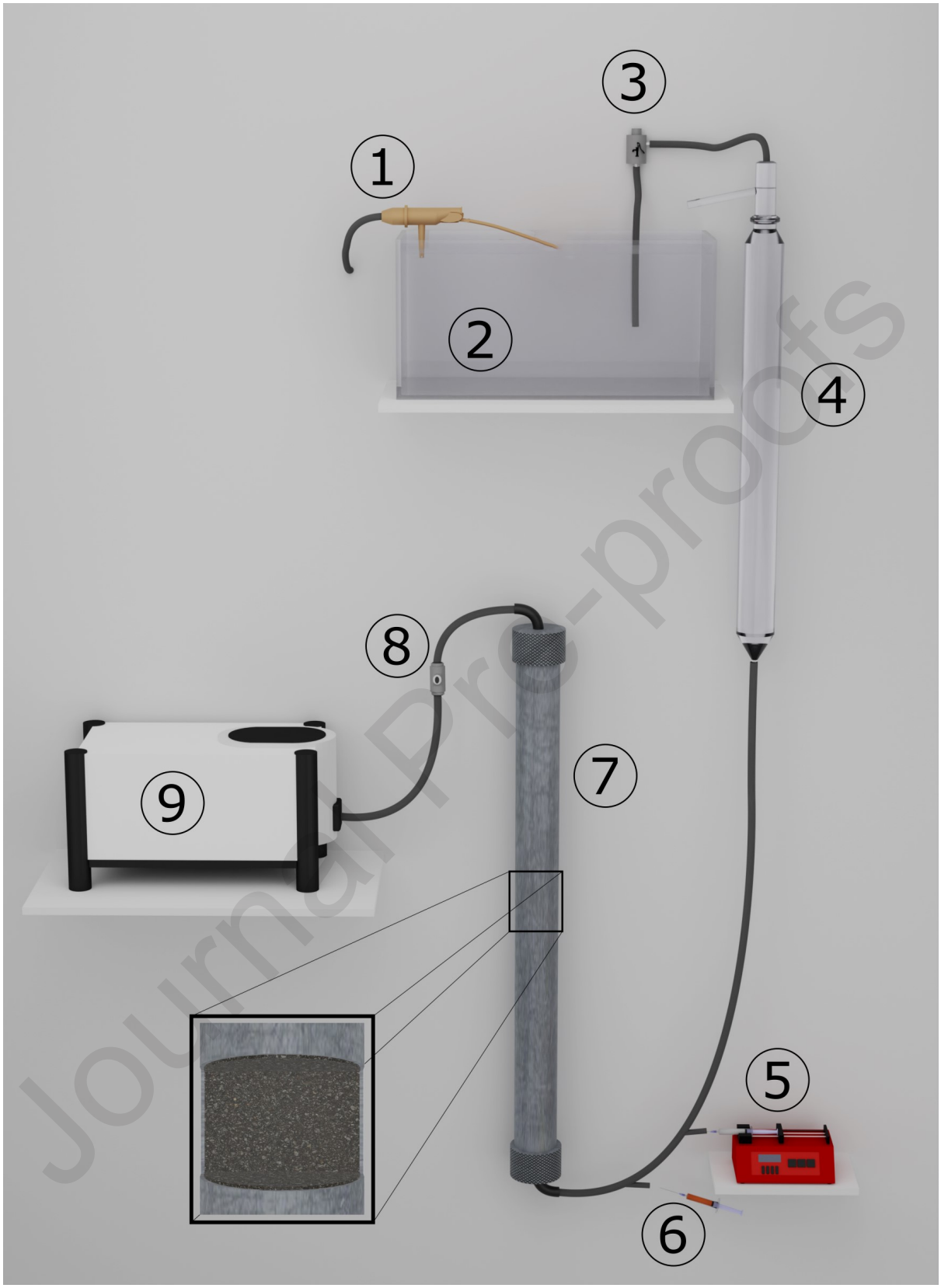

668

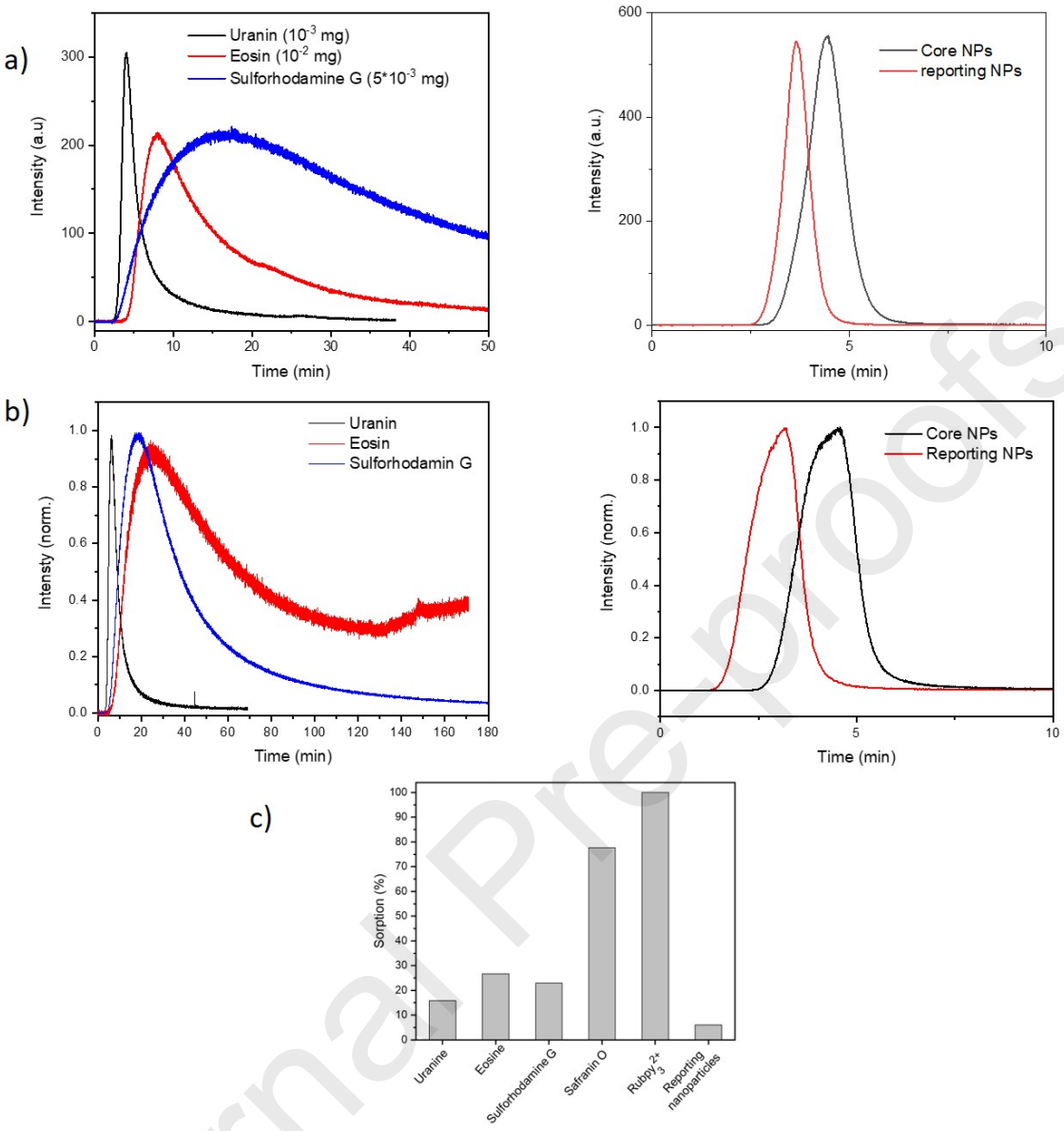

669

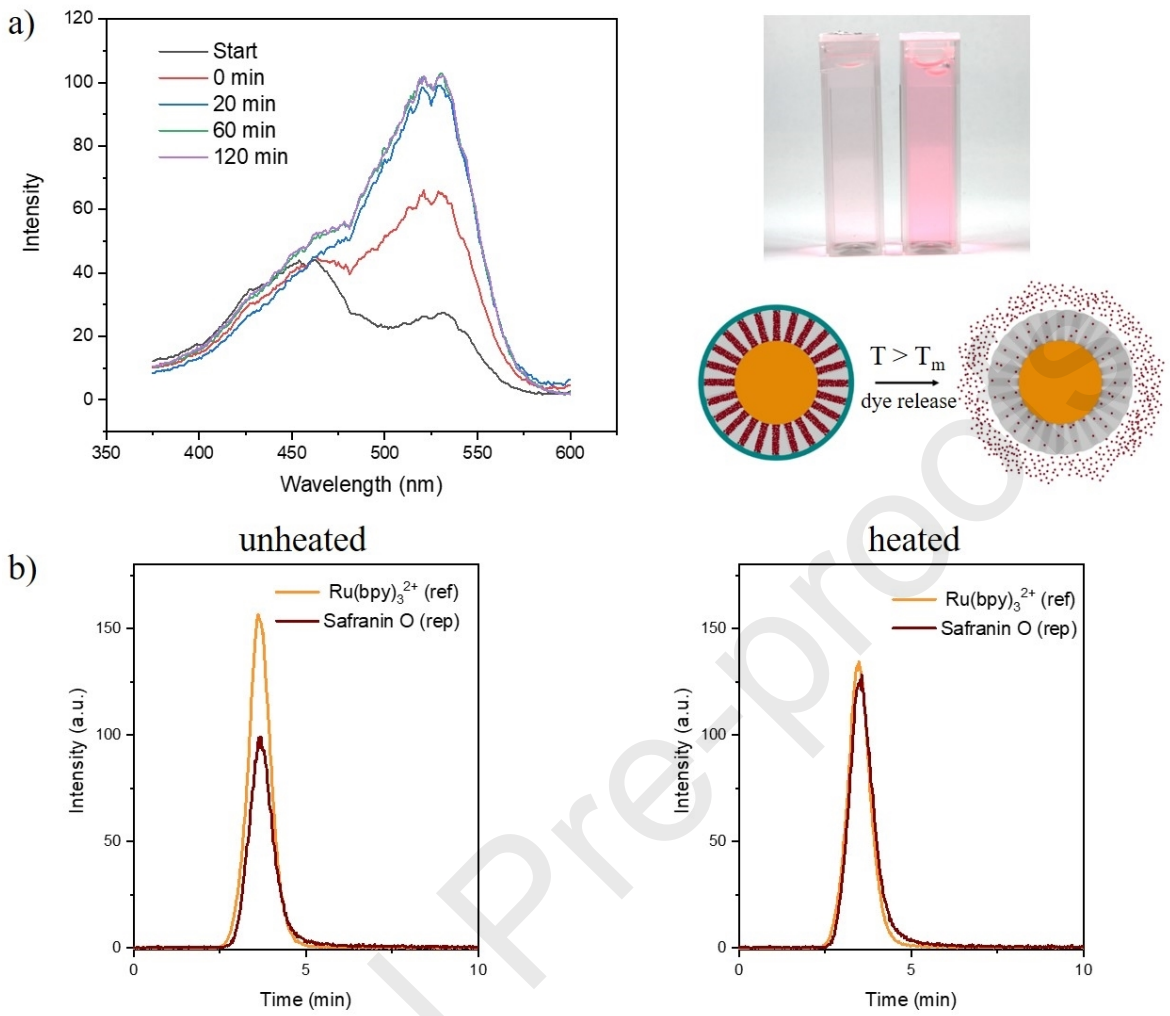

670

Transportability and temperature detection of
Reporting Nanoparticle Tracers in Flow-through Experiments

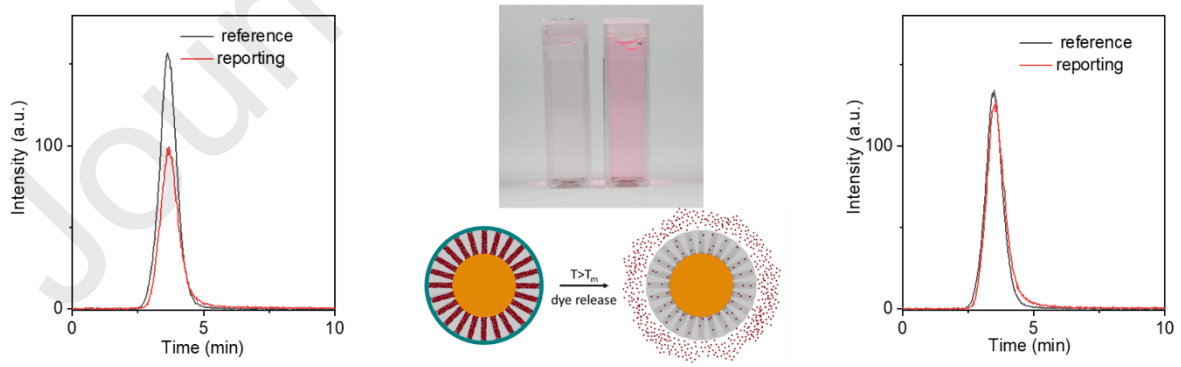

671

672• Reporting Nanoparticle Tracers (RNT) were developed to detect ambient
673 conditions

674

- RNT aim to enhance & expand data acquired in tracer tests of subsurface reservoirs

- RNT performance is validated in tests simulating reservoir conditions

- In flow-through setups, RNT performance is on-par with prevalent conservative tracers

- Temperature detection: Temperature-activated/unreacted RNTs are distinguishable